JGR Atmospheres

RESEARCH ARTICLE
10.1029/2023JD039520

Lightning Characteristics Associated With Storm Modes Observed During RELAMPAGO

Marquette N. Rocque[1], Wiebke Deierling[2,3], Kristen L. Rasmussen[2], Rachel I. Albrecht[4], and Bruno L. Medina[5]

[1]Atmospheric, Climate, and Earth Sciences (ACES) Division, Pacific Northwest National Laboratory, Richland, WA, USA, [2]Department of Atmospheric Science, Colorado State University, Fort Collins, CO, USA, [3]National Center for Atmospheric Research, Boulder, CO, USA, [4]Departamento de Ciências Atmosféricas, Instituto de Astronomia, Geofísica e Ciências Atmosféricas, Universidade de São Paulo, São Paulo, Brazil, [5]Department of Geosciences, Atmospheric Science Group, Texas Tech University, Lubbock, TX, USA

Key Points:

- Lightning characteristics associated with storm life cycles are analyzed using a lightning mapping array in subtropical South America
- Lightning flashes in deep convection are smaller in size, shorter in duration, and are less energetic compared to flashes in stratiform
- Rapid increases in lightning flash rates are associated with increases in graupel and hail within the convective cores

Correspondence to:
M. N. Rocque,
marqi.rocque@pnnl.gov

Citation:
Rocque, M. N., Deierling, W., Rasmussen, K. L., Albrecht, R. I., & Medina, B. L. (2024). Lightning characteristics associated with storm modes observed during RELAMPAGO. *Journal of Geophysical Research: Atmospheres*, *129*, e2023JD039520. https://doi.org/10.1029/2023JD039520

Received 23 JUN 2023
Accepted 27 JAN 2024

Abstract Global satellite studies show a maximum in deep convection and lightning downstream of the Andes in subtropical South America. The Remote sensing of Electrification, Lightning, And Mesoscale/microscale Processes with Adaptive Ground Observations (RELAMPAGO) field campaign was designed to investigate the physical processes that contribute to the rapid development of deep convection and mesoscale convective systems (MCSs) in Argentina. A lightning mapping array (LMA) was deployed to Argentina as part of RELAMPAGO to collect lightning observations from extreme storms in the region. This study combines lightning data from the LMA and the Geostationary Lightning Mapper onboard *GOES-16* with 1-km gridded radar data to examine the electrical characteristics of a variety of convective storms throughout their life cycle observed during RELAMPAGO. Results from the full campaign show 48% of flashes are associated with deep convection that occurs along the eastern edge of the Sierras de Córdoba (SDC) overnight. These flashes are 65 km^2 smaller on average compared to stratiform flashes, which occur most frequently 50–100 km east of the SDC in the early morning hours, consistent with the upscale growth of MCSs off the terrain. Analysis of the 13–14 December MCS shows that sharp increases in flash rates correspond to deep and wide convective cores that have high graupel and hail mass, 35-dBZ volume, and ice water path. This work validates previous satellite studies of lightning in the region, but also provides higher spatial and temporal resolution information across the convective life cycle that has not been available in previous studies.

Plain Language Summary Satellites have shown a hotspot in extreme lightning in subtropical South America that is associated with some of the deepest thunderstorms on Earth. A ground-based lightning observing platform was deployed to central Argentina to better understand the characteristics and three-dimensional structure of lightning in the region and how lightning flashes vary with storm intensity and life cycle. Results show the majority of lightning flashes are associated with the deepest, widest, and most intense parts of the storms. These flashes are concentrated near the higher terrain and tend to occur most frequently in the evening and overnight hours. Further analysis of a case study shows that a rapid increase in lightning activity is related to an increase in graupel and hail mass in the column below the flash centers. We find lightning characteristics including flash area, duration, and energy vary as the storm evolves and can be separated into distinct periods when the storm is developing, maturing, and decaying.

1. Introduction

A better understanding of global lightning distributions has been a subject of interest for the past several decades. Knowledge of current global lightning distributions and their variations by climate regime and storm type is important for understanding how these distributions may change in the future as a result of climate change. Several satellite studies have documented the global climatology of lightning and have attempted to estimate global flash rates. Using the Optical Transient Detector (OTD) onboard *MicroLab-1* (*OrbView-1*), which was one of the first instruments specifically designed to measure lightning, Christian et al. (2003) found hot spots in lightning flash rates along the coasts, in mountainous regions, and in the Congo basin. Other studies such as Zipser et al. (2006) and Albrecht et al. (2016) found maxima in lightning flash rates in the Congo basin and Lake Maracaibo in Venezuela, as well as downstream of mountain ranges, including the Andes in subtropical South America, using the Lightning Imager Sensor (LIS) onboard the Tropical Rainfall Measuring Mission (*TRMM*;

Kummerow et al., 1998) satellite. In particular, storms in subtropical South America have the highest lightning flashes per precipitation feature (PF) compared to any other location observed by *TRMM* (Zipser et al., 2006). More recently, Peterson et al. (2021) used OTD and LIS to analyze the global climatology of flash extent density, which includes the spatial extent of lightning. Their results agree with previous studies that have looked at global flash rates, naming coastal and mountainous regions as lightning hot spots. Furthermore, analysis of diurnal variations in flash extent densities show nocturnal to early morning moderate-to-high lightning activity in areas downstream of mountain ranges such as the central-southern U.S. Great Plains, northern Argentina, Southeast Asia, and West Africa (Albrecht et al., 2016).

Deep convection is also known to occur downstream of mountain ranges around the world (Houze et al., 2015; Zipser et al., 2006). This includes downstream of the Andes in subtropical South America where convection often rapidly grows upscale into mesoscale convective systems (MCSs; Rasmussen & Houze, 2011, 2016; Rasmussen et al., 2014, 2016). This convection is associated with extreme weather, including flash flooding, large hail, tornadoes, and megaflashes (Bruick et al., 2019; Cecil & Blankenship, 2012; Peterson, 2021b; Rasmussen et al., 2014; Zipser et al., 2006). It is hypothesized that the Andes and the Sierras de Córdoba (SDC) support a favorable environment for deep convection and rapid upscale growth of MCSs in subtropical South America (Rasmussen & Houze, 2011, 2016; Romatschke & Houze, 2010). Westerly flow over the Andes induces lee cyclogenesis, which strengthens the pressure gradient and enhances the South American Low-Level Jet (Vera et al., 2006), that transports moisture from the Amazon into the region. The South American Low-Level Jet collides with the SDC and other Andes foothills, and convection rapidly develops, leading to extreme weather across the higher terrain as well as farther east across the La Plata Basin as MCSs propagate off the terrain.

The collocation of deep convection and high lightning flash rates in subtropical South America was studied by Rasmussen et al. (2014) who analyzed the spatial and temporal patterns of lightning associated with different convective storm modes. They found lightning flash rates are highest in the deepest and widest convection, which occurs along the SDC in the late evening and early morning hours (20–02 LT). Other studies from the U.S. and Australia have similarly found high correlations between deep convection and lightning (Williams et al., 1992; Zipser & Lutz, 1994). Unfortunately, satellite studies of deep convection in subtropical South America were not able to capture the individual storm life cycles, given the low Earth orbit of *TRMM*. To collect higher spatial and temporal resolution data of intense deep convection in subtropical South America, several instruments were deployed to Córdoba, Argentina as part of the Remote sensing of Electrification, Lightning, And Mesoscale/microscale Processes with Adaptive Ground Observations (RELAMPAGO; Nesbitt et al., 2021) and Cloud, Aerosol, and Complex Terrain Interactions (CACTI; Varble et al., 2021) field campaigns. The intensive observing period (IOP) of RELAMPAGO and CACTI occurred in November and December of 2018, but some instruments continued to operate through April 2019. This IOP timing corresponds to the most intense lightning activity over the SDC (Rasmussen et al., 2014).

One of the key platforms deployed during RELAMPAGO was a very high frequency (VHF) lightning mapping array (LMA; Rison et al., 1999) operated by National Aeronautics and Space Administration George C. Marshall Space Flight Center (Lang et al., 2020). This was a regional ground-based total (in-cloud and cloud-to-ground) lightning observing platform deployed in subtropical South America that had very high lightning detection efficiency with the goal of validating satellite-based lightning observations, particularly from the Geostationary Lightning Mapper (GLM; Goodman et al., 2013; Rudlosky et al., 2019) onboard *GOES-16*. Lang et al. (2020) provided an initial overview of the data collected by the LMA network. They found flashes occur most frequently at 10 km in height, have areas of 0–50 km^2, and last for less than 0.5 s. Additionally, the diurnal cycle of flashes is bimodal with peaks at 17 and 00 LT. This diurnal cycle matches well with previous satellite studies (Rasmussen et al., 2014; Ávila et al., 2015) but provides a more temporally cohesive picture of how flashes evolve within storms.

This work aims to further analyze flash characteristics observed by the RELAMPAGO LMA as a function of storm mode based on ground-based radar observations, similar to the analysis done by Rasmussen et al. (2014) using LIS and OTD. These three-dimensional storm modes represent the most extreme vertical and horizontal components of storms and provide valuable information regarding the life cycle of convective events, including MCSs, in the region. In addition to a campaign-wide analysis of storm modes and associated flash characteristics, a detailed analysis of the evolution of lightning and microphysics associated with the 13–14 December 2018 MCS is presented. The goal of this case study analysis is to demonstrate the wide variety of flashes that can occur within

a single convective system, and how rapidly flash characteristics can change with radar-derived microphysical properties such as graupel volume and ice water path (IWP). Several aspects of this case have been studied in depth by Rocque and Rasmussen (2022) and Rocque (2023), including the impact of the Andes and SDC on the synoptic-scale environment and convective characteristics. Rocque and Rasmussen (2022) found that the Andes play a significant role in the development of the MCS by creating a lee cyclone near the SDC and enhancing the South American Low-Level Jet. Rocque (2023) also showed that several back-building episodes of deep convection are related to the collision of cold pools with the SDC. Our goal is to extend this research by analyzing the electrical and microphysical properties of these storms to better understand why convection and associated lightning in this region are so intense.

2. Data and Methodology

2.1. Radars

The Colorado State University C-band, dual-polarization radar (CHIVO) is used in this analysis to identify PFs (see Section 2.2) and better understand the microphysical characteristics of storms in subtropical South America. CHIVO was deployed near Córdoba, Argentina for the RELAMPAGO field campaign from 10 November 2018 through 31 January 2019 (Arias et al., 2019). The radar conducted 360° plan position indicators (PPIs), 135° sector scans (SEC), and range height indicators (RHIs), with update cycles every 5–10 min depending on precipitation events within the 150 km range. Due to its proximity to the SDC, CHIVO is blocked below 1–1.5° elevation to the west (~240–300° azimuth). There is also significant clutter at the lowest elevations to the north and east of CHIVO that is addressed in the quality-control (QC) process.

After data collection, a QC procedure was developed and applied to the CHIVO dataset. This procedure included azimuth, attenuation, and differential reflectivity corrections, and the application of normalized coherent power and correlation coefficient thresholds to remove non-meteorological data and clutter. An additional QC procedure was applied to the 13–14 December 2018 strongly forced MCS case to remove remaining clutter associated with the SDC. The removal of clutter was achieved by running the National Center for Atmospheric Research (NCAR) particle identification (PID) algorithm (Vivekanandan et al., 1999). The NCAR PID algorithm was used because it has specific categories for non-meteorological echoes including insects, second trip, and clutter.

After QC was performed, the PPI and SEC data were interpolated to a 1 km horizontal resolution and 0.5 km vertical resolution grid using the Radx2Grid application in the Lidar Radar Open Software Environment (LROSE; Bell et al., 2022). This method uses three-dimensional linear interpolation and is best suited for fixed, ground-based radars (Miller & Fredrick, 1999). After the data were gridded, a hydrometeor identification (HID) algorithm developed for C-band radar (Dolan et al., 2013) was applied to the interpolated dataset. Soundings from the Atmospheric Radiation Measurement Mobile Facility (AMF1) near Villa Yacanto (about 75 km southwest of CHIVO) were matched with the closest CHIVO time to retrieve the temperature profile. The HID algorithm categorizes data into 10 groups, but this work is focused on bulk microphysical characteristics related to lightning. Thus, we classify the data into three groups: graupel and hail, snow, and ice. The graupel and hail category contains low density graupel, high density graupel, and hail, while the snow category contains wet snow and aggregates, and the ice category contains ice crystals and vertically aligned ice. While these three bulk categories are all forms of ice, all discussion of ice mass and/or volume hereafter is specifically referring to ice crystals and vertically aligned ice. After the data is categorized, Z-M relationships are applied to calculate hydrometeor masses. These relationships were first derived by Heymsfield and Palmer (1986) and Heymsfield and Miller (1988) and have been used in other lightning studies including Deierling et al. (2008):

$$M_{graupel} = 0.0052 \times Z^{0.5} \quad (1)$$

$$M_{hail} = 0.000044 \times Z^{0.71} \quad (2)$$

$$M_{snow/ice} = 0.017 \times Z^{0.529} \quad (3)$$

where M is in g m^{-3} and Z is in mm^6 m^{-3}. All hydrometeor categories are then vertically integrated through the column above −5°C to retrieve IWP (kg m^{-2}). Other Z-M relationships have been derived in different regions of

the world including the U.S. and Japan, but none have been developed in subtropical South America. Deierling et al. (2008) compared several different Z-M relationships and found that although the magnitudes of graupel and ice mass can vary (sometimes by up to 1–2 orders of magnitude), the trends of masses are all the same. Thus, we use the same Z-M relationship used in Deierling et al. (2008) which is based on convection in the U.S.

2.2. Storm Mode Identification

To better understand how lightning varies with different storm modes, a PF identification algorithm, developed by Rocque (2023), was employed. This algorithm is based on previous algorithms used in *TRMM* satellite studies (Liu et al., 2008; Liu & Zipser, 2013; Nesbitt et al., 2000, 2006) and works by fitting an ellipse to the region of interest. In this work, PFs are identified where contiguous echoes of 3–5 km MSL composite reflectivity are greater than 0 dBZ. The height threshold of 3 km was chosen to remove any impacts from remaining clutter and to eliminate any biases that may have been introduced from full or partial beam blockage due to the SDC. A convective/stratiform partitioning based on the Steiner et al. (1995) algorithm was applied to the gridded CHIVO dataset also from 3 to 5 km MSL. The upper height threshold of 5 km is the approximate height of the melting level. Radar statistics associated with each PF are then calculated including echo top height and area. Radar parameters that are related to lightning are also calculated including graupel, hail, snow, and ice mass and volumes.

In addition to PFs, three-dimensional storm modes are also identified to more closely track storm characteristics in space and time. These storm modes have been used in *TRMM* satellite studies (Houze et al., 2007, 2015; Rasmussen & Houze, 2011, 2016; Romatschke & Houze, 2010) and ground-based studies (Rocque, 2023; Zuluaga & Houze, 2013) to evaluate the life cycle of MCS events. For this analysis, we use the strong-intensity storm thresholds defined in Houze et al. (2015). Deep convective cores (DCCs) have 40-dBZ convective echoes at least 10 km above MSL, wide convective cores (WCCs) have contiguous 40-dBZ convective areas greater than 1,000 km^2, and broad stratiform regions (BSRs) have contiguous stratiform areas greater than 50,000 km^2. Additionally, if a feature satisfies both DCC and WCC criteria, it is considered a deep and wide convective core (DWCC). Radar statistics including feature area are also output for each storm mode. Given the size of the CHIVO radar domain, the size threshold associated with BSRs was modified to 10,000 km^2 for this study as was done in Rocque (2023). This PF identification algorithm was applied to the CHIVO gridded dataset which includes PPI and SEC scans. SEC scans account for approximately 20%–25% of the entire dataset and were most often scanning over the SDC (200–300° azimuth) when deep convection was nearby. Although the dataset is biased with more samples to the west, we decided to include SEC scans in the analysis because deep convection and the flashes associated with deep convection would have otherwise been underrepresented.

2.3. LMA

Ground-based observations of lightning were collected by a LMA (Rison et al., 1999) which was deployed near Córdoba, Argentina as part of the RELAMPAGO field campaign (Lang et al., 2020). The LMA consisted of 11 stations which were operating from November 2018 through April 2019, and it detects electromagnetic radiation emitted by lightning at VHF. LMA-detected VHF sources were mapped in three dimensions using a time-of-arrival technique (Proctor, 1971), where at least 6 stations detected the source and the chi-square goodness of fit value (Thomas et al., 2004) was less than 5.0 (Lang et al., 2020). Lang et al. (2020) tested a variety of other chi-square values and station requirements but found this combination was the best minimum threshold. Due to the station configuration, horizontal errors in location within 100 km of the network are estimated to be less than 100 m while vertical errors are less than 1 km. After sources were mapped, they were clustered into flashes if they were within 150 ms or 3 km of each other (Fuchs et al., 2016; Lang et al., 2020). This was accomplished with the lmatools software developed by Bruning et al. (2014). The maximum duration allowed for a flash was 3.0 s, which Lang et al. (2020) found was appropriate given the longest flash observed in their dataset was 2.6 s and did not appear to be split. Megaflashes are known to occur in this region though, and a megaflash detected by GLM in March of 2019 was also partially mapped by the LMA (Peterson et al., 2020). While these flashes are likely rare in this dataset, it is possible that flashes occur for longer than 3.0 s.

Flash characteristics including centroid location, area, duration, and total energy are analyzed for each PF and three-dimensional storm mode identified by CHIVO. A flash was considered part of a PF or storm mode if the centroid was within the PF or storm mode bounds anytime during the radar scan. Flashes that occurred outside of

the PPI or SEC scans were not included in the analysis. Flash rates are also analyzed for the case study and are calculated by summing the number of flashes centered within each PF over the time between the current and next radar scan, and dividing by the scan cycle, usually 10 min.

2.4. GLM

One purpose for the deployment of the LMA during RELAMPAGO was to provide ground-based validation of GLM onboard *GOES-16*. Thus, we briefly compare flash characteristics between LMA and GLM for the case study. GLM detects lightning emissions at 777.4 nm through its 1,372 × 1,300 pixel Charge Coupled Device focal plane (Goodman et al., 2013). The footprint of GLM varies from 8 km at nadir to 14 km at the edges and is roughly 10 km over subtropical South America. Lightning pulses that occur within a footprint over 2 ms are called an event. The Lightning Cluster and Filter Algorithm LCFA then clusters simultaneous and adjacent events into groups. Groups are then clustered into flashes if they occur within 330 ms or 16.5 km from one another (Goodman et al., 2013). Due to the real-time nature of the LCFA, longer flashes (>3 s or more than 101 groups) can be split up. To account for these megaflashes, we use the L2-CIERRA product which regroups flashes using larger duration and area thresholds, allowing for longer flashes (Peterson, 2019a, 2019b, 2021b).

After comparing LMA flash centroid locations with GLM flash centroid locations for a few cases, it was determined an additional parallax correction needed to be applied to the GLM data. The level 2 cloud top height product from the *GOES-16* Advanced Baseline Imager (Schmidt et al., 2017) was used to calculate the median cloud height across the CHIVO radar domain. This height was then used to adjust the latitude and longitude of the flash centroids using equations described in Vicente et al. (2002). GLM flashes that were located within PFs identified by CHIVO for the 13–14 December case were then analyzed.

3. Campaign-Wide Lightning Statistics

3.1. Overview

A campaign-wide analysis of lightning characteristics associated with storm modes identified by CHIVO is presented first. Figure 1 shows a time series of LMA lightning flashes with at least 10 sources within 100 km of the network collocated with PFs identified by CHIVO during the RELAMPAGO time period. Several cases are easily identified, including the multi-day supercell-MCS event on 10–12 November (IOPs 4 and 5), the 13–14 December MCS (IOP17) and the 25–26 January MCS which exhibited the deepest convective core from the entire campaign (40 dBZ echo >20 km). In fact, the latter two cases have the highest lightning flash counts during the time frame, consistent with findings from Lang et al. (2020). In addition to flash counts, graupel and hail volumes identified by CHIVO are also shown. Graupel and hail volume tracks well with flash counts, particularly in December and January. However, graupel and hail volumes are much higher in the beginning of November compared to the relative number of flashes observed. One possible reason for this lower number of flashes is that the number of operational LMA stations was less than 10 until around 26 November (Lang et al., 2020). In particular, only 7 stations were operational during the 10–12 November IOPs. While this is above the minimum number of stations needed to detect a flash in this analysis (6), there is a drop in the number of flashes detected when fewer stations are operational. Thus, fewer flashes were detected by the LMA network in early November.

3.2. Storm Modes

The identification of storm modes, and the lightning flashes associated with them, provides insight into the life cycle of convective systems in the region. Previous analysis of lightning frequency in central Argentina has shown that flashes associated with deep convection occur most frequently over the higher terrain, including the SDC, in the evening hours (Rasmussen et al., 2014). Using high spatial and temporal resolution data from the LMA network, the location and timing of lightning flashes with at least 10 sources associated with storm modes observed during RELAMPAGO within 100 km of the LMA network are analyzed. We also analyzed lightning flashes with 3–10 sources and found similar results in the timing and location of these flashes. To understand how flashes vary within PFs and storm modes, the location of features identified by CHIVO is also analyzed. Figure 2 shows the frequency map of PF and storm mode locations (left) and LMA flashes with at least 10 sources centered within a PF or storm mode (right). The greatest number of pixels associated with a PF occur just downstream of the highest terrain of the SDC (Figure 2a). Lightning flashes associated with these PFs occur most frequently in the same area, although slightly offset to the east (Figure 2b). This slight discrepancy could indicate that cells

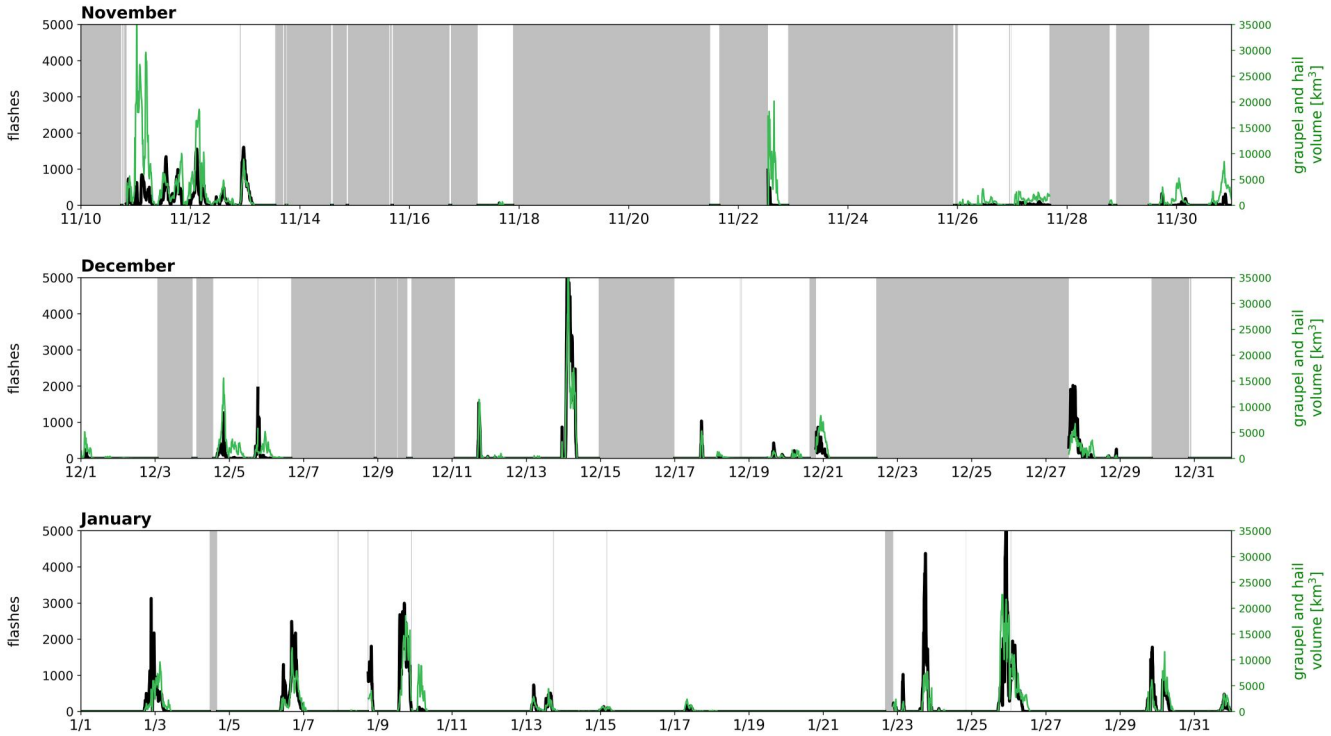

Figure 1. Time series of LMA flashes (≥10 sources; black) and graupel and hail volume (green; km^3) associated with CHIVO PFs within 100 km of the LMA network. Gray regions indicate when the radar was turned off.

initiate along the highest terrain of the SDC, but do not develop deep enough to produce lightning until later in time. This location of higher lightning flashes corresponds well with the highest frequency of DCCs and DCC flashes (Figures 2c and 2d). Nearly 30% of all flashes identified within a PF are also identified within a DCC (Table 1). Additionally, on average there is one flash every 2.4 km^2 within DCCs. In contrast, fewer pixels are associated with WCCs, and there is a broad maximum in WCCs along the SDC in the western portion of the CHIVO domain (Figure 2e). Fewer flashes are associated with WCCs too, and there are scattered pockets of WCC flashes with a larger maximum near the radar center about 25 km east of the SDC (Figure 2f). Very few WCCs were identified during RELAMPAGO, and the average flash density is about one flash per 67 km^2 (significantly smaller than DCCs). DWCCs, on the other hand, have a higher flash density with one flash observed every 2.8 km^2 on average. The majority of DWCCs occur along the SDC but can be observed 25–50 km downstream of the SDC as well (Figure 2g). Interestingly, the most flashes associated with DWCCs occur slightly north of the radar center off the terrain (Figure 2h). These flashes are east of DCC flashes, consistent with the upscale growth of MCSs off the terrain with the highest flash rates along the topography (Rasmussen et al., 2014). About 19% of all flashes identified within a PF are also associated with a DWCC (Table 1). Finally, BSRs are widespread across the domain, but BSR flashes have a maximum about 50–100 km east of the SDC (Figures 2i and 2j). This pattern is also consistent with the upscale growth of MCSs off the terrain. On average, one flash is observed every 345 km^2 within BSRs, and flashes associated with BSRs account for just over 10% of all flashes (Table 1). One caveat with the identification of storm modes is that there are only two categories in the Steiner et al. (1995) algorithm. Several thresholds need to be met for an area to be classified as convective, but there are no thresholds for an area to be considered stratiform, so the stratiform classification can be overestimated. Some flashes occur along the edge of convection, which the algorithm will classify as stratiform and which could be incorporated into BSRs. A third classification between convective and stratiform such as "mixed" would likely reduce the number of stratiform flashes but is currently beyond the scope of this study. Additionally, this study uses the flash centroid to group flashes based on storm modes. If a flash initialized in a convective region but propagated away from convection, it could be considered a stratiform flash. To investigate this effect further, a sensitivity test was performed where flashes were identified using their initialization points instead of centroid points. While the total

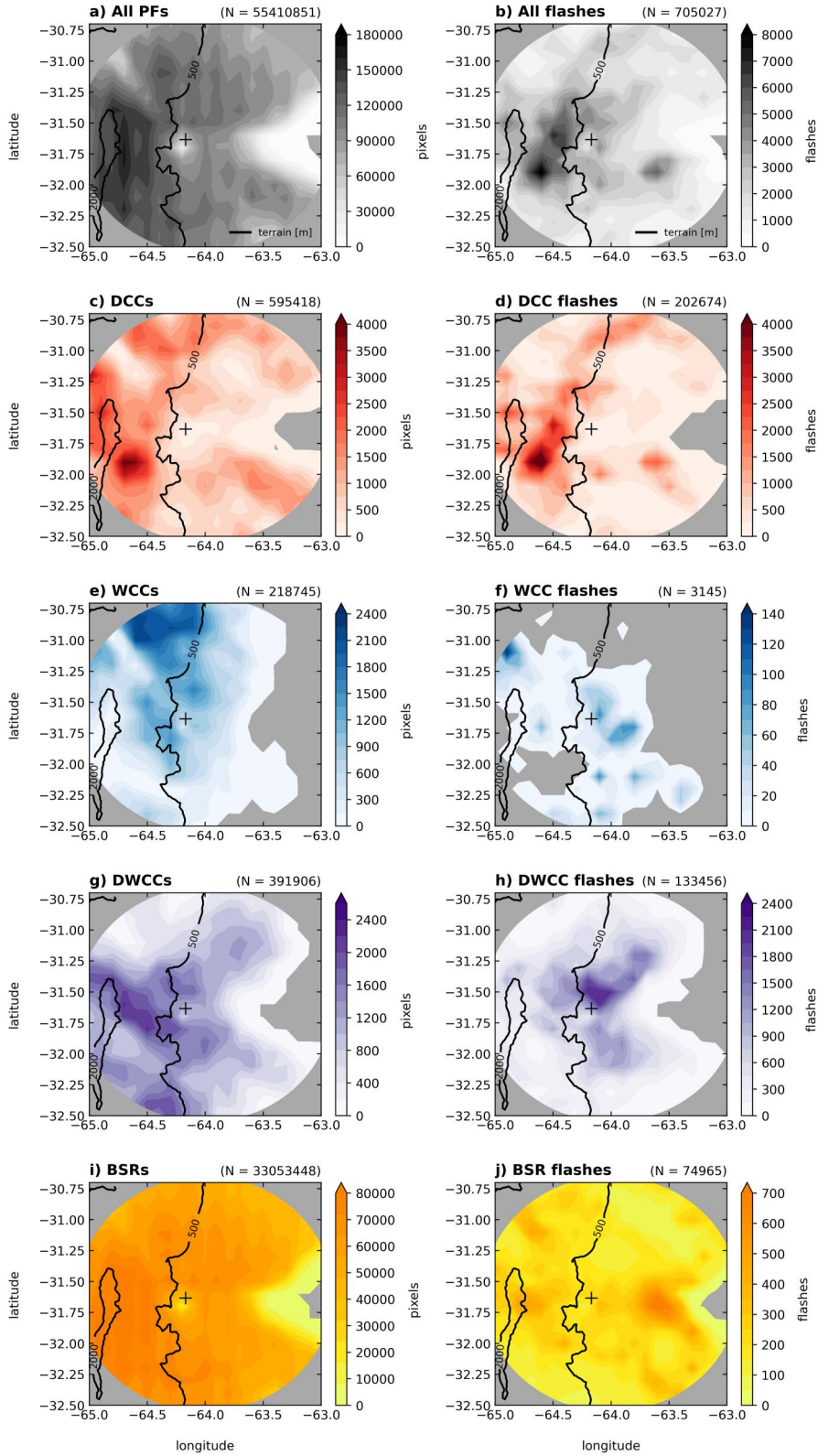

Figure 2. (left) Location of pixels associated with (a) PFs, (c) DCCs, (e) WCCs, (g) DWCCs, and (i) BSRs. (right) Location of LMA flashes with at least 10 sources centered within (b) PFs, (d) DCCs, (f) WCCs, (h) DWCCs, and (j) BSRs for the CHIVO dataset. The total number of pixels (left) and flashes (right) is shown in the upper right of each plot. The 500 and 2000 m terrain contours are shown in black, the "+" indicates the location of CHIVO, and the analysis is limited to within 100 km of the LMA network.

Table 1
Number of Flashes Associated With Each Feature (PF, DCC, WCC, DWCC, BSR), the Average Feature Area (km^2), and the Percentage of Total Flashes

	PF	DCC	WCC	DWCC	BSR
Number of flashes	705,027	202,674	3,145	133,456	74,965
Average feature area (km^2)	893	175	1,787	2,023	23,610
Percentage of total flashes		28.70%	0.40%	18.90%	10.60%

number of flashes did change for each storm mode with this method detecting more DCC and DWCC flashes and less BSR flashes, the spatial distributions of the flashes were still similar.

To analyze the diurnal cycle of flashes associated with storm modes, the timing of PFs and flashes and their location relative to the SDC are shown in the time-longitude plots in Figure 3. The main maximum in PFs occurs around 04–06 UTC (01–03 LT) and extends from the higher terrain of the SDC to the Plains (Figure 3a). The maximum in lightning flashes for all PFs occurs along the edge of the SDC in the afternoon hours (14–17 LT; Figure 3b). This maximum extends along the SDC and to the east of the SDC. A secondary maximum occurs around midnight local time farther east. There is a minimum in lightning flashes that occurs in the morning hours from 05 to 09 LT. This diurnal cycle agrees with that found by Lang et al. (2020) using the full LMA dataset. DCCs are mostly found along the SDC in the afternoon hours as well (14–19 LT; Figure 3c). DCC flashes occur in a similar location, although slightly more east, and also are most frequently observed in the afternoon (Figure 3d). The main peak in WCCs occurs in the early morning hours around 04–08 UTC (01–05 LT) and is fairly widespread over the lower terrain of the SDC (Figure 3e). Interestingly, WCC flashes tend to occur at the beginning of WCC development around 01 LT and are observed farther east off the terrain (Figure 3f). WCCs could represent a transition phase from deep convection to stratiform. Early in the WCC life cycle, lightning flashes are still high from the decaying deep convection. As the WCC continues to evolve though, lightning flashes decrease, and more back-building along the SDC may be observed. Indeed, DWCCs are observed most frequently an hour or two before WCCs around midnight local time (Figure 3g). These features have a strong connection to the terrain, as was observed in Figure 2g. Lightning flashes associated with DWCCs align well with DWCC pixels (Figure 3h). Two maxima in DWCC flashes are identified, one maximum around 18–20 LT downstream of the SDC and a second wider maximum that extends from the highest terrain of the SDC to the eastern edge of the SDC around midnight local time. This again highlights the upscale growth and movement of features off the terrain from deep convection to deep and wide convection to wide convection. Finally, BSRs are most prevalent in the early morning hours and extend from the SDC to 100 km east (Figure 3i). About 60% of all pixels associated with a PF are also associated with a BSR which explains why the distributions in Figures 3a and 3i are similar. Stratiform flashes similarly occur throughout most of the day but have two frequency maxima in the early afternoon hours and in the early morning hours (Figure 3j). The first maximum in the afternoon begins west of the SDC around noon local time and extends to the eastern edge of the SDC around 16 LT. This maximum is mainly associated with one case, 6 January 2019. The second maximum that occurs around midnight and extends through 04 LT is associated with MCSs that have propagated eastward over the Plains. These results generally agree with Rasmussen et al. (2014), although the hotspot in DCC flashes is shifted later in the evening in their analysis.

Distributions of flash area, flash duration, flash energy, and flash height are also examined to provide insight into the electrical characteristics of each storm mode (Figure 4). In terms of flash area, the majority of all flashes identified with each storm mode occur within the first bin (0–100 km^2). This agrees well with Lang et al. (2020), as well as with storms observed in the U.S. in Washington D.C., northern Alabama, and eastern Colorado (Fuchs et al., 2016). Upon further investigation, we find that flashes associated with WCCs (Figure 4b) and BSRs (Figure 4d) have higher mean flash areas (43.4 and 79.6 km^2, respectively) compared to DCCs (Figure 4a) and DWCCs (Figure 4c; 14.7 and 15.8 km^2, respectively). The opposite is true when looking at flash durations. The most frequent flash duration is between 0.1 and 0.3 s, which is also similar to storms in the U.S (Fuchs et al., 2016). The mean flash duration for DCCs (Figure 4e) and DWCCs (Figure 4g) are 0.275 and 0.288 s, respectively. The mean flash durations for WCCs (Figure 4f) and BSRs (Figure 4h) are 0.240 and 0.239 s, respectively. Although the average flash duration is lowest in BSRs, the maximum flash duration of 2.6 s was associated with a BSR flash. The distribution of flash energy is most similar to the distribution of flash area. This makes sense as the flash energy is proportional to flash area (Bruning & MacGorman, 2013). The majority of

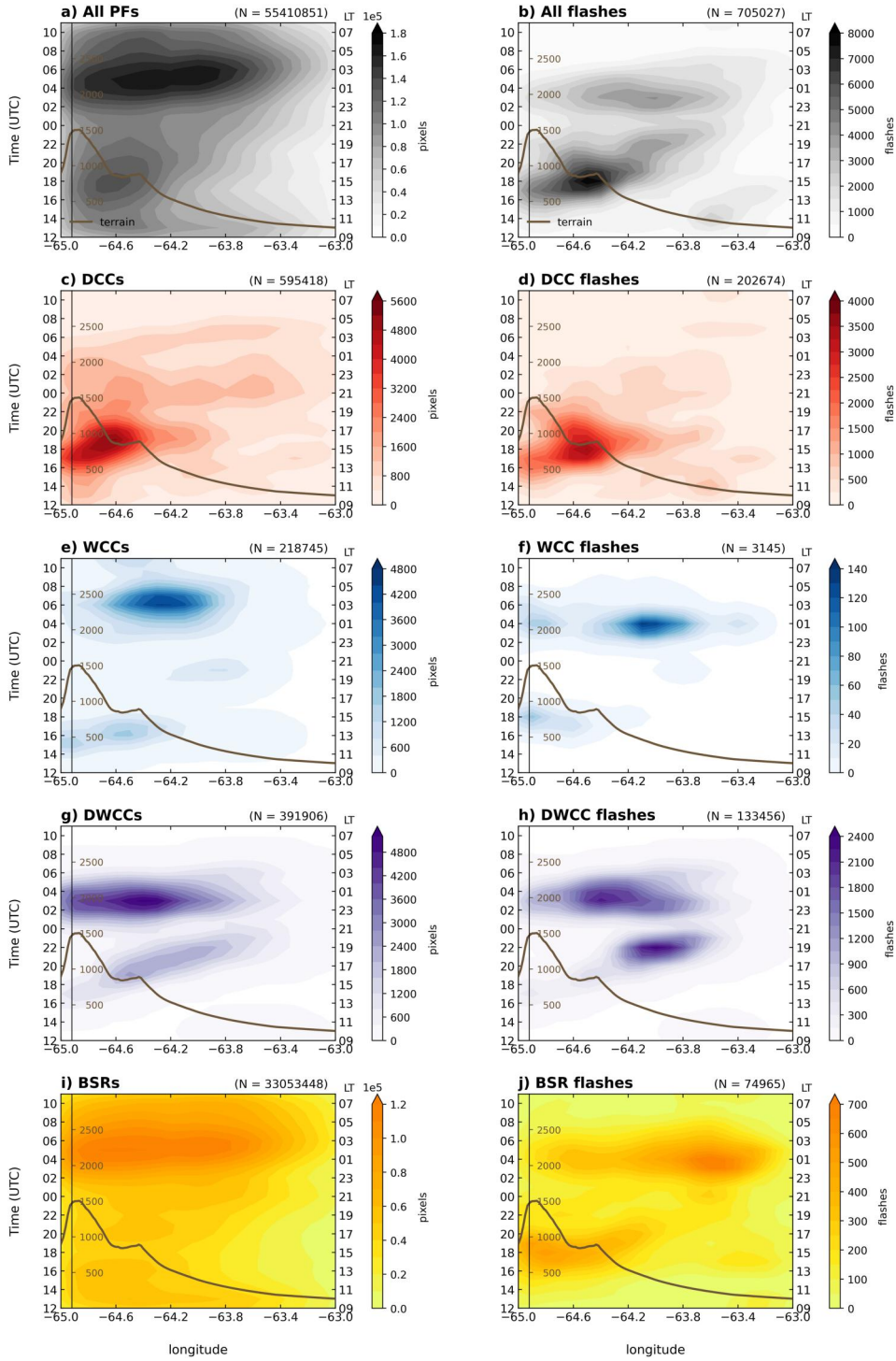

Figure 3. Time-longitude plots of (left) (a) all PFs, (c) DCCs, (e) WCCs, (g) DWCCs, and (i) BSRs and (right) LMA flashes with at least 10 sources centered within (b) PFs, (d) DCCs, (f) WCCs, (h) DWCCs, and (j) BSRs for the CHIVO dataset. The total number of pixels (left) and flashes (right) is shown in the upper right of each plot. The average terrain profile across the CHIVO latitude band is shown in dark brown and a terrain height axis is included for reference. The local time (UTC-3) is shown on the right axis.

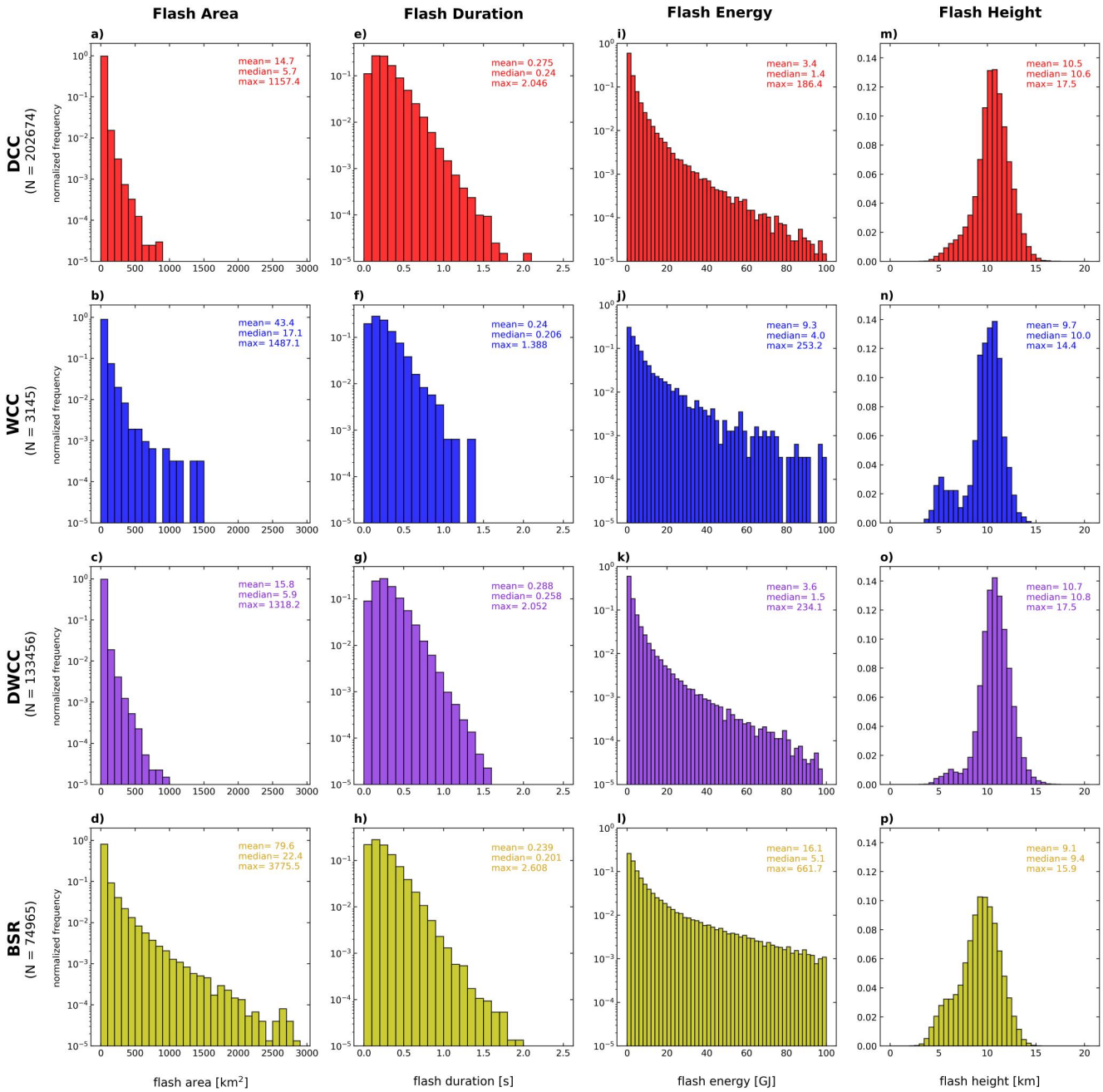

Figure 4. Histograms of (a–d) flash area (km^2), (e–h) flash duration (s), (i–l) flash energy (GJ) and (m–p) flash centroid height (km) for flashes centered within DCCs (red; first row), WCCs (blue; second row), DWCCs (purple; third row), and BSRs (yellow; fourth row) for the CHIVO dataset. Mean, median, and maximum values are shown in the upper right of each panel and the number of flashes is shown at the top of each column.

flashes produce 1 GJ of energy, while the maximum energy produced was 662 GJ associated with a BSR flash. Mean flash energies are 6–11 GJ lower, on average, in DCCs (Figure 4i) and DWCCs (Figure 4k) compared to WCCs (Figure 4j) and BSRs (Figure 4l). Finally, the highest frequency of flash centroid heights occurs at 10–12 km, consistent with analysis from Lang et al. (2020), and with storms observed in Washington D.C. and northern Alabama (Fuchs et al., 2016). DCCs (Figure 4m) and DWCCs (Figure 4o) have higher mean flash heights compared to WCCs (Figure 4n) and BSRs (Figure 4p). Additionally, there is a secondary relative maximum in flash heights observed in WCCs and BSRs at around 6 km. This was also noted in Lang et al. (2020), who attributed this secondary maximum to anomalous polarity storms and stratiform flashes. Indeed, the flash

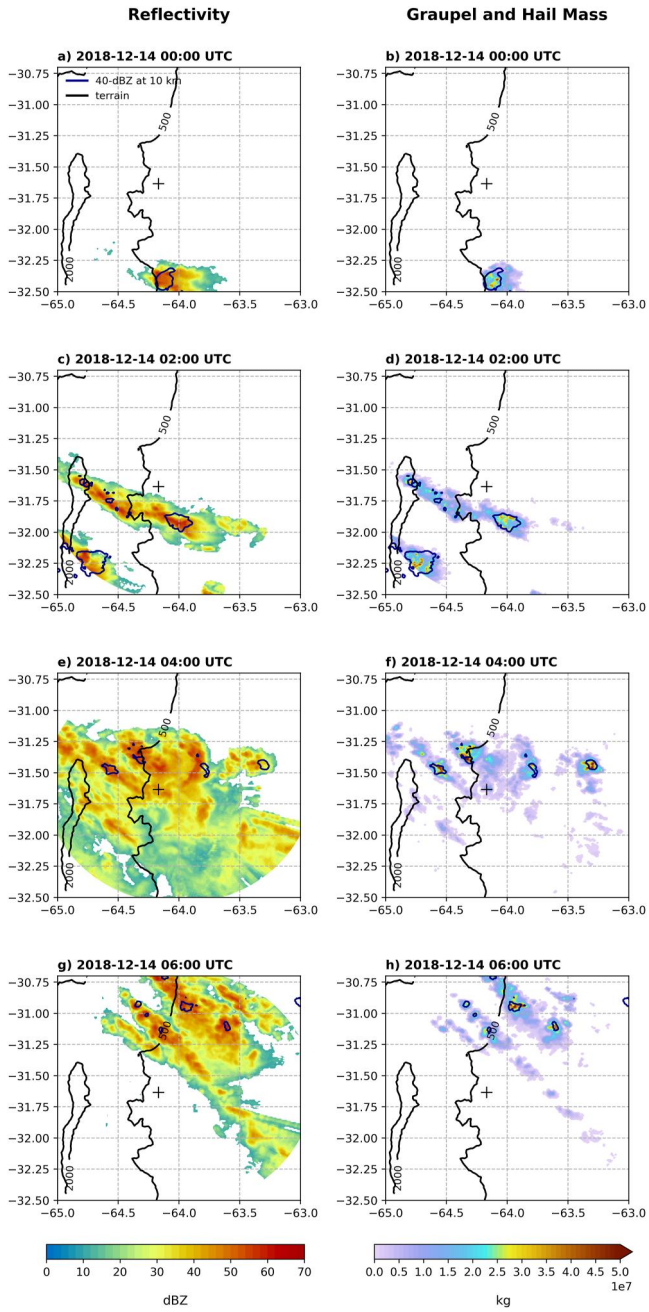

Figure 5. 3–5 km MSL composite reflectivity (left) and graupel and hail mass summed above the −5°C level (right) every two hours starting at 0000 UTC on 14 December. 40-dBZ echoes at 10 km above MSL are shown in the navy contours while the 500 and 2000 m terrain contours are shown in black. The "+" indicates the location of CHIVO.

height distribution associated with BSRs is shifted toward lower heights compared to distributions from convective storm modes, consistent with lower cloud top heights and horizontally extensive charge regions (Stolzenburg et al., 1994, 1998).

3.3. RELAMPAGO Lightning Summary

Flashes associated with PFs and storm modes observed by CHIVO were analyzed for the RELAMPAGO time frame. The location and timing of flashes associated with storm modes agrees fairly well with previous research using satellite-based observations (Rasmussen et al., 2014). DCC flashes occur along the higher terrain of the SDC in the early afternoon and evening hours. They are typically smaller in size and occur higher in the convection. DWCC flashes occur along the eastern edge of the SDC and are most frequent overnight, consistent with the life cycle of MCSs. These flashes also tend to be smaller and occur higher in the convection. WCC flashes, although infrequent, occur farther east compared to deep convective flashes, and they tend to be larger in size, have larger energy associated with them, and occur slightly lower in the storm. Finally, BSR flashes occur most frequently 50–100 km east of the SDC in the early morning hours. These flashes have large footprints, produce large amounts of energy, and occur more frequently at lower altitudes. These characteristics are consistent with previous studies based on U.S. storms (Bruning et al., 2019; Bruning & MacGorman, 2013; Mecikalski et al., 2015).

Several IOPs and convective episodes with upscale growth stood out in the time series of flash counts, including the 13–14 December 2018 case (Figure 1). About 16% of all flashes that were associated with CHIVO PFs occurred during this case, as well as 8.2% of all DCC flashes, 43.1% of all DWCC flashes, and 9.1% of all BSR flashes. We further examine this case to better understand the electrical characteristics of some of the most intense convection on Earth.

4. Case Study: 13–14 December 2018 MCS

4.1. Overview

The 13–14 December 2018 case featured a severe MCS that was associated with hail, flooding, and high lightning flash rates in the Córdoba region. Detailed analyses of the synoptic and mesoscale characteristics of this case can be found in Rocque and Rasmussen (2022) and Rocque (2023). This case occurred under strong synoptic flow, including a deep upper-level trough, a strong South American Low-Level Jet, and a strong cold front (Rocque & Rasmussen, 2022). DCCs and DWCCs were prevalent across the case and volumetric rain rates were particularly high (Rocque, 2023).

Spatial maps of reflectivity and graupel and hail mass summed for temperatures colder than −5°C are shown in Figure 5. At 0000 UTC on 14 December, one isolated cell is visible off the southern SDC (Figure 5a). This cell has 40-dBZ echoes that extend to 10 km height and is associated with graupel and hail mass above 2.0×10^7 kg and peaks of 4.0×10^7 kg (Figures 5a and 5b). Two hours later, the convective line develops just south of Córdoba (Figure 5c). There is also a larger system to the southwest, and the graupel and hail mass is mostly concentrated over the SDC, with a larger area of above 2.5×10^7 kg (Figures 5c and 5d). At 0400 UTC, a large MCS has developed across the radar domain (Figure 5e). There are pockets of higher graupel and hail mass ($>4.0 \times 10^7$ kg) that align well with the deepest convection (Figures 5e and 5f). By 0600 UTC, the majority of the MCS has moved to the northeast out of the radar domain (Figure 5g). There are still some intense lines of convection that remain tied to the SDC related to backbuilding characteristics that are also associated with enhanced graupel and hail (Figures 5g and 5h).

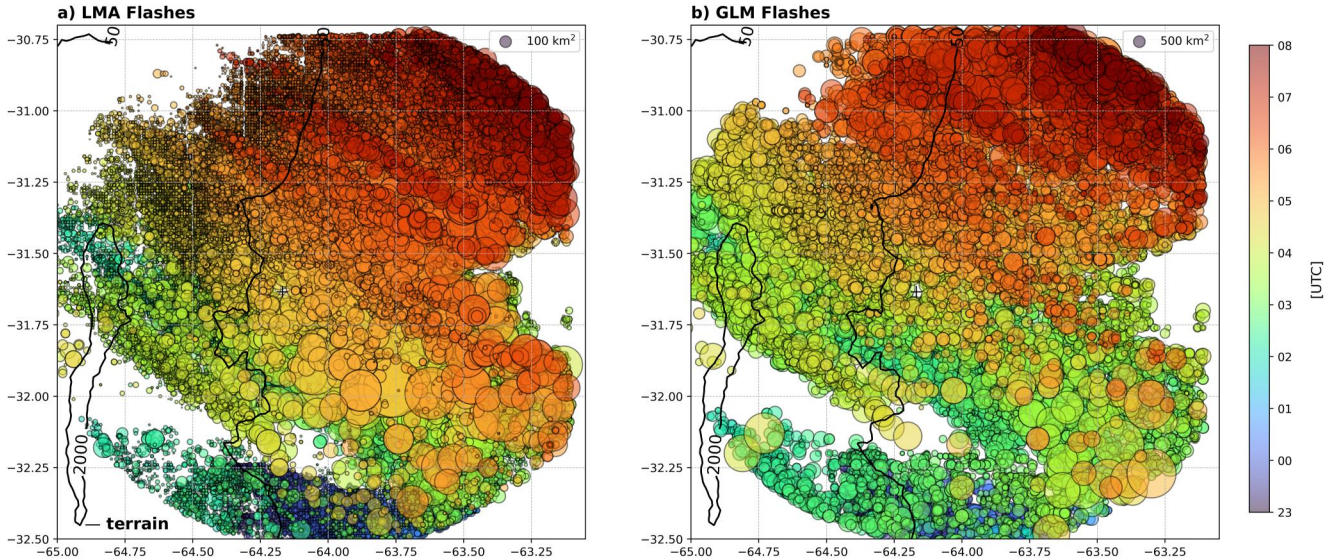

Figure 6. Location of (a) LMA flash centroids and (b) GLM flash centroids during the 13–14 December 2018 case. Markers are colored by time (UTC) and sized by flash area (km^2). The 500 and 2000-m terrain contours are plotted in black.

The evolution of lightning flashes throughout the MCS is shown in Figure 6. At first glance, LMA and GLM flash locations and timing appear to agree well. There is an isolated cell that develops off the southern SDC on 13 December and moves eastward out of the domain (Figure 5a). While there are a few GLM flashes that occur in the southern portion of the domain before 01 UTC, there are much more LMA flashes. An intense line of convection then rapidly develops around 0130 UTC south of Córdoba along the SDC (Figure 5c). This convective line quickly grows upscale into a large MCS by 0230 UTC and continues to propagate to the northeast until it exits the radar domain around 0800 UTC. The LMA observes much smaller flashes over the SDC, likely associated with deeper convection. Larger LMA and GLM flashes are observed farther east toward the Plains.

4.2. Microphysics

Lightning forms as a result of the separation of charged particles within the atmosphere. Hydrometeors such as graupel and ice crystals carry different charges depending on several different factors including temperature, liquid water content, and particle size (Ávila & Pereyra, 2000; Reynolds et al., 1957; Saunders & Peck, 1998; Takahashi, 1978). Knowing what type of hydrometeors are present in the mixed phase and where they occur is critical for better understanding the electrical characteristics of convective storms. Thus, microphysical parameters calculated above the −5°C level including 35-dBZ volume, IWP, and graupel, hail, snow, and ice mass and volumes were derived from CHIVO and compared with lightning observations. The evolution of PF total microphysical and electrical characteristics is shown in Figure 7. IWP, 35-dBZ volume, graupel and hail volume and mass, and snow and ice mass increase from the start of the event to their maximum around 0230–0300 UTC on 14 December (Figures 7a and 7b). This corresponds to increases in LMA flash rates, with a large jump occurring between 0130 and 0250 UTC, particularly for the smaller flashes (3–10 sources; Figure 7d). GLM flash rate also increases during this period, but the rates are much lower than LMA flash rates (Fuchs, 2017). The most rapid increase actually occurs with GLM event rates. After around 0300 UTC, flash rates start to decrease, along with 35-dBZ volume and graupel and hail mass and volume. Meanwhile, snow and ice volume peaks around 0430 UTC and then steadily declines afterward (Figure 7c). IWP also decreases, but not as steeply as the graupel and hail components, highlighting the presence of more snow and ice aloft. PF total LMA flash areas reach maximum values after the peak in flash rates, around 0330–0530 UTC (Figure 7e). LMA total flash energy follows a similar trend as flash area (Figure 7f). Interestingly, PF total GLM flash area and optical energy reach maximum values around 0230 UTC, consistent with the maximum in flash rates (Figures 7d–7f; Fuchs, 2017). Average LMA and GLM flash durations tend to increase throughout the MCS life cycle, consistent with the transition from convection to stratiform (Figure 7g).

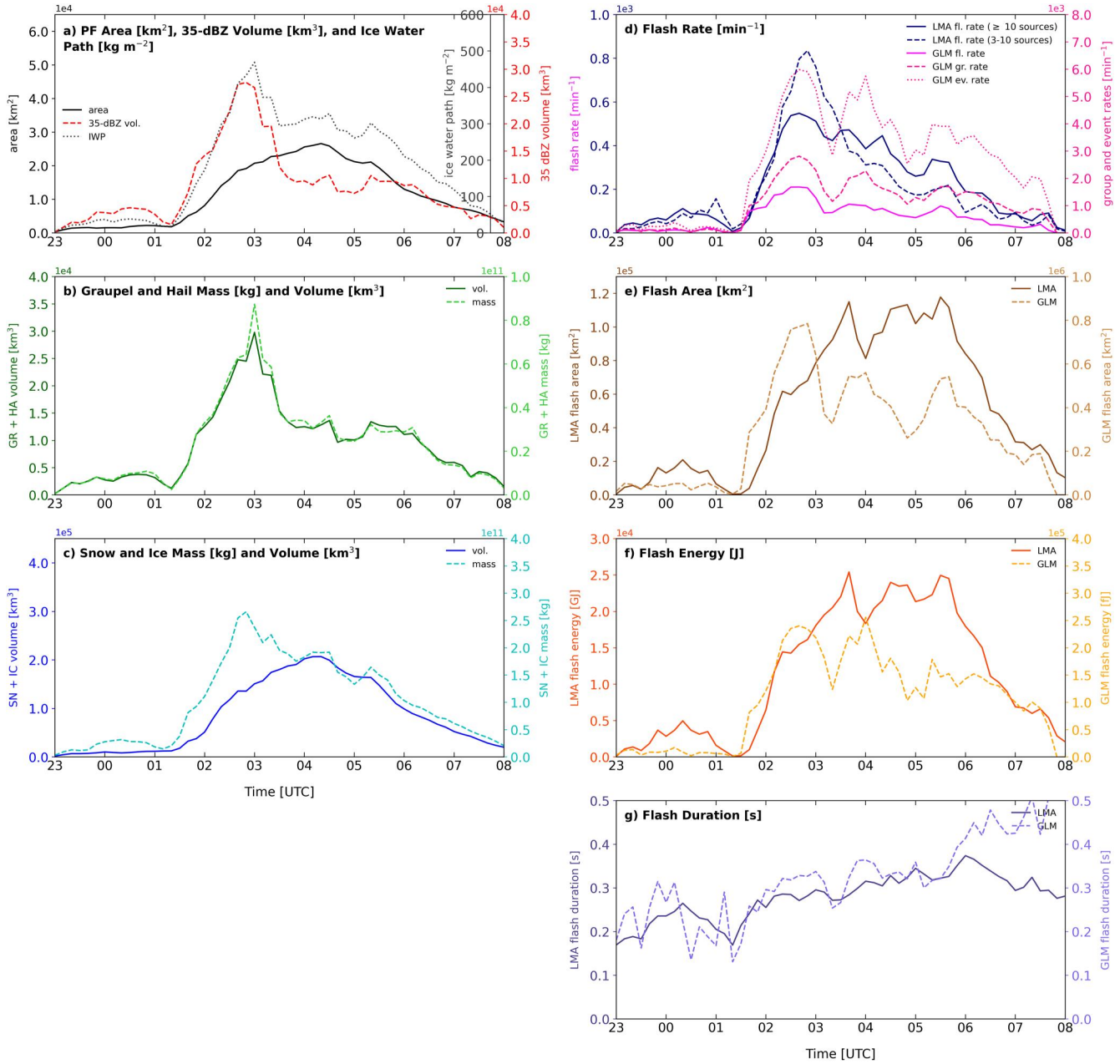

Figure 7. Time series of (a) PF area (km^2; solid black), 35-dBZ volume (km^3; dashed red), and IWP (kg m^{-2}; dotted gray), (b) graupel and hail mass (kg; dashed light green) and volume (km^3; solid green), (c) snow and ice mass (kg; dashed light blue) and volume (km^3; solid blue), (d) LMA flash rates (≥10 sources, min^{-1}; solid navy, 3–10 sources, min^{-1}; dashed navy), GLM flash rates (min^{-1}; magenta), GLM group rates (min^{-1}; dashed pink) and GLM event rates (min^{-1}; dotted pink), (e) LMA flash area (km^2; solid brown) and GLM flash area (km^2; dashed brown) summed over each PF, (f) LMA flash energy (GJ; solid orange) and GLM flash energy (fJ; dashed orange) summed over each PF, and (g) LMA average flash duration (s; solid blue-purple) and GLM average flash duration (s; dashed blue-purple) during the 13–14 December 2018 case. All parameters shown here are summed or averaged across the PFs observed at each volume scan of the radar.

The location of hydrometeors within the cloud can provide insight into the charge structure of the storm and lightning characteristics. Thus, the evolution of hydrometeors through the MCS life cycle by height is examined. Early in the time period when more isolated cells are developing, graupel, hail, snow, and ice masses are relatively low (Figure 8). There is an increase in flash rates, particularly for LMA flashes, as well as an increase in the 0-dBZ and 40-dBZ echo top heights. As the convective line develops around 0130 UTC, flash rates start to increase considerably. Additionally, graupel and hail mass increases near the freezing level, with maximum values reaching to about 7 km (Figure 8a). This coincides with LMA flash rates of 550 flashes min^{-1} at 0230 UTC. Ice

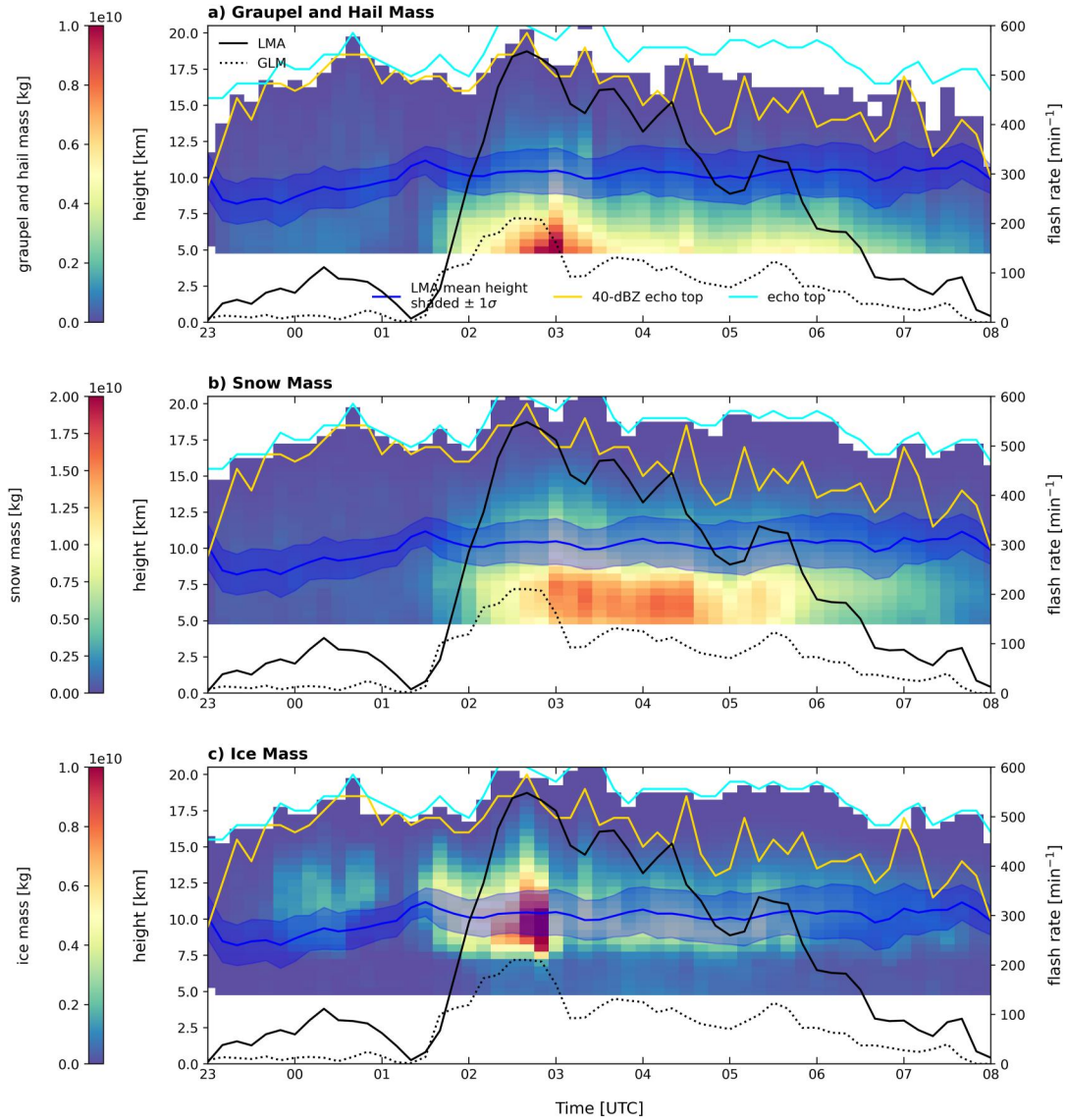

Figure 8. Time series of (a) graupel and hail mass by height (kg; shaded), (b) snow mass by height (kg; shaded), and (c) ice mass by height (kg; shaded) for the 13–14 December 2018 case. Hydrometeor masses are summed above the −5°C level. Each plot also shows the mean LMA flash height (km; blue) with ±one standard deviation shaded, 40-dBZ echo top height (km; gold), echo top height (km; cyan), LMA flash rate (min^{-1}; solid black), and GLM flash rate (min^{-1}; dashed black).

mass also begins to increase at this time and has peak values just before 0300 UTC centered around 9–10 km (Figure 8c). The mean flash height observed by the LMA is also around 10 km during this time. Snow mass is highest around 0300–0500 UTC and extends from the melting level to around 10 km (Figure 8b). After the peak in lightning flash rates occurs around 0230 UTC, flash rates decrease steadily, as do the 0-dBZ and 40-dBZ echo tops. GLM flash rates follow a similar trend as LMA flash rates but are much smaller. This could be due to optical attenuation caused by hydrometeors, especially ice, above the mean flash height (Fuchs, 2017; Rutledge et al., 2020).

As shown in previous studies (e.g., Bruning et al., 2007; Bruning & Thomas, 2015; Mecikalski et al., 2015), the temporal progression of flash characteristics trends shown in Figures 7 and 8 clearly serve as an indicator of the stage in the life cycle of a storm and can be divided into three distinct intervals as suggested by Bruning et al. (2007). Initially, as the convection becomes established (2300–0100 UTC), flash rate slowly increases (Figure 7d), flashes propagate more vertically within the updraft, and flash centroids are lower in height (mean at or below 8 km;

Figure 8), leading to relatively small flash area and shorter flash durations (Figure 7g). Subsequently, a modulation period ensues (0100–0200 UTC), when flash rates and LMA flash areas and durations decrease. However, the height of the flash centroids increases (mean reaches 11 km; Figure 8), indicating an increase in the height of charge centers and predominance of intracloud lightning closer to the cloud top. This shift in flash heights closer to cloud top may be the reason why GLM shows the opposite trend in this period, with larger flash areas, duration, and energy (Figures 7d–7g). Emissions from lightning closer to cloud top are more visible from space and thus GLM detection efficiency is likely greater during this time. The sharp increase in lightning flash rates occurs thereafter, when a continuous column of graupel and hail mass greater than 5.0×10^9 kg is observed from 5 to 12 km in height (Figure 8a), sustaining higher flash rates for one hour (0130–0230 UTC). Following this (after 0330 UTC), the MCS enters its decay phase. Flash area and duration continue to be large, with flash centroids in a broader range of heights (increased standard deviation observed in Figure 8). Examining the energy trends, LMA energy levels are higher in the decaying stage (after 0330 UTC) while flash rate decreases. This suggests that energy previously stored within the storm is dissipated with a time delay with the continuation of stratiform precipitation.

It is important to notice that GLM shows a slightly different trend in flash area, duration, and energy. GLM detection efficiency is dependent on flash height and amount of hydrometeor mass between the flash and cloud top (Lang, 2023; Peterson, 2021a; Rutledge et al., 2020). GLM flash area and energy (Figures 7e and 7f) peak before the IWP peak (Figure 7a) and the extended graupel and hail mass column (Figure 8a) around 0300 UTC. During the decaying stage (after 0330 UTC), flashes detected by the LMA are lower in height, and GLM flash area and energy decrease.

4.3. Storm Modes

As mentioned earlier, three-dimensional storm structures that represent the most extreme components of the storm are analyzed to better understand the evolution of systems, particularly MCSs. To put this case into context with the entire campaign, the locations and timing of lightning flashes associated with storm modes observed by CHIVO are shown in Figure 9. Flashes associated with DCCs occur throughout the entirety of the MCS (Figure 9a). A large number of flashes (>700) occur within the isolated cell in the southern half of the domain early on 14 December (Figures 9a and 9b). Flashes associated with these DCCs are small in size, short in duration, and occur lower in the convection compared to later time periods (not shown). A hotspot in flashes south of the CHIVO radar corresponds to the location of the convective line around 0200–0300 UTC (Figure 5c). Several flashes are also observed over the highest terrain of the SDC around 0400 UTC. These flashes are also small in size (0–100 km^2) and short in duration. Flashes then move with the deepest convection to the northeast, and average DCC flash area, duration, and energy increases (not shown).

Flashes that occur within DWCCs are observed from about 0200 UTC to 0800 UTC (Figures 9c and 9d). These flashes are closely tied to the terrain and move to the northeast with the MCS. Additionally, 46% of all flashes observed during this event were associated with a DWCC. The highest concentration of DWCC flashes is directly north of CHIVO right along the edge of the SDC. Average DWCC flash areas are smaller in the developing and mature phase of the MCS (0130–0400 UTC; 12 km^2) compared to later in the MCS life cycle (22 km^2). DWCC flash energy and duration similarly increase through the MCS life cycle (not shown).

BSR flashes occur across the domain from about 0230 to 0700 UTC (Figures 9e and 9f). There are likely more stratiform flashes that occur through the end of the MCS, but the size threshold for BSRs is not met when the system exits the domain. The majority of BSR flashes occur about 50–100 km east of the SDC, consistent with the movement of the MCS toward the east as it matures. These flashes are significantly larger than convective flashes (on average, 55 km^2 vs. 15–20 km^2). There is also a subset of BSR flashes that occur lower in the convection (around 5–6 km) toward the end of the MCS event (not shown). The flash characteristics associated with these storm modes clearly highlight the life cycle of the MCS.

4.4. Summary

The 13–14 December MCS case produced the most lightning of all cases observed by the LMA network and CHIVO. A deeper analysis into this case showed that the majority of these flashes were associated with the deepest, most intense components of the MCS (DWCCs). These flashes were relatively small in size (<100 km^2), generally lasted for 0.3 s, and occurred most frequently around 10 km. A rapid increase in lightning flash rates was observed and was related to increases in the graupel and hail mass and volume, 35-dBZ volume, and IWP. The

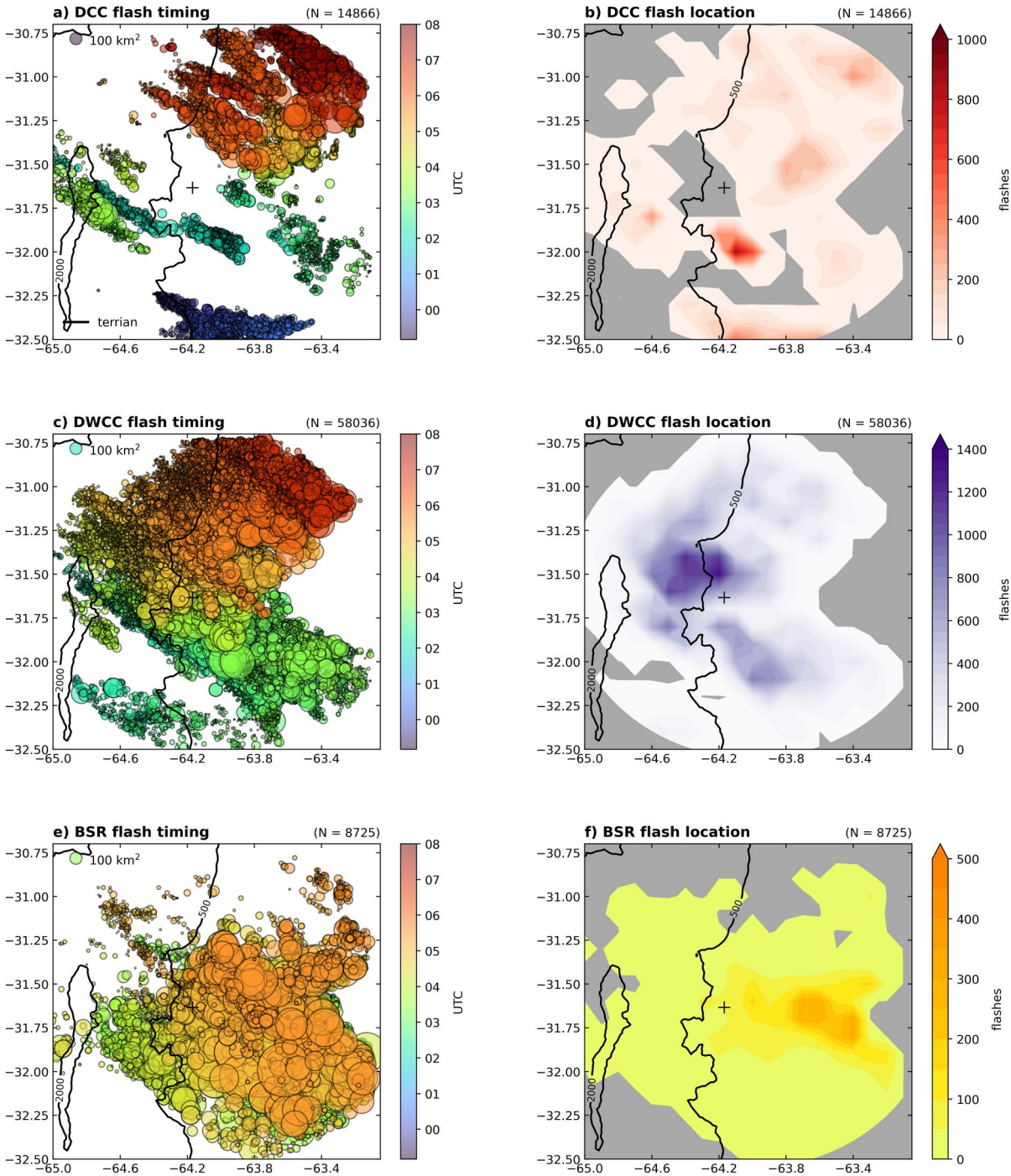

Figure 9. Location of LMA flashes centered within (a) and (b) DCCs, (c) and (d) DWCCs, and (e) and (f) BSRs for the 13–14 December 2018 case. Markers in the left panels are colored by time (UTC) and sized by flash area (km^2). Total number of flashes observed within a $0.1° \times 0.1°$ pixel are shown in the right panels. The number of flashes is shown in the upper right of each plot. The 500 and 2000 m terrain contours are shown in black and the "+" indicates the location of CHIVO. No WCCs were identified during this case.

time evolution of flash characteristics follows the stage in the life cycle of the MCS and the development over time of the three storm modes.

Flashes were also identified by GLM and correspond well in time and space compared to the LMA. However, flash rates observed by GLM were much lower than the LMA. This may be due to the small flash size or the

occurrence of the flashes around 10 km. The echo top heights are around 18 km, and thus optical attenuation through the upper part of the cloud is likely. Lang (2023) found GLM detection efficiency during RELAMPAGO decreased with LMA flash rate and flash height. Additional analysis could be performed to determine if GLM detection varies based on storm mode.

5. Conclusions

Ground-based lightning observations in central Argentina were combined with ground-based radar data to identify extreme three-dimensional storm structures and associated lightning characteristics in a variety of events observed during the RELAMPAGO field campaign. The use of these fixed platforms also allows for high temporal and spatial resolution analyses of individual storms. General lightning characteristics associated with each storm mode including location, timing, size, and duration are analyzed for all features identified during RELAMPAGO. Lightning flashes are most frequently associated with deep and wide convection (DWCCs). These flashes occur along the eastern edge of the SDC in the overnight hours. The location and timing of these flashes agrees well with previous studies that have used data from *TRMM* (Rasmussen et al., 2014). However, the use of the LMA and ground-based radar provides more details into the electrification of storms in the region and their evolution with respect to storm characteristics, microphysics, and detailed lightning flash characteristics. In particular, flashes in deep convective cores tend to be smaller in size and occur higher within the cloud compared to flashes within wide convective cores and stratiform areas, which are typically larger in extent and occur lower within the cloud. These flash characteristics have been documented in other storms, especially in the U.S., but not in subtropical South America, to our knowledge.

In addition to a campaign-wide analysis, a case study was analyzed in depth to better understand the relationship between the electrification and microphysics of MCSs in subtropical South America and demonstrate how these characteristics can rapidly change throughout the MCS life cycle. The case recorded lightning flash rates >600 fl min^{-1} and exhibited sharp increases in lightning associated with storm intensification and the upscale growth of convection within the MCS. This rapid increase in lightning corresponded to an increase in graupel and hail mass and volume, 35-dBZ volume, and IWP. While GLM saw lightning flashes in similar locations, GLM lightning flash rate was significantly lower than LMA. This may be explained by the high presence of hydrometeors in the mixed phased and/or the higher frequency of smaller flashes observed. Results from this case study show how lightning varies throughout the life cycle of an intense MCS common in subtropical South America.

This work has validated previous studies that have investigated the location and timing of lightning flashes associated with storm modes and demonstrates the unique nature of convection in subtropical South America. This is the first analysis of how lightning characteristics such as flash heights, areas, and intensities vary throughout the storm life cycle in subtropical South America. The use of high-resolution datasets deployed during RELAMPAGO has been useful in determining how convection and lightning are influenced by the terrain, particularly the SDC, in this region. Future work using dual-Doppler analysis will provide more information on the updrafts associated with these storms and the relationship between kinematic, microphysics, and electrification of storms in subtropical South America. Additional analyses of how lightning characteristics vary with storm life cycle in other regions of the world such as Colorado in the U.S. should be completed to further evaluate the uniqueness of convection in subtropical South America.

Data Availability Statement

CHIVO level 1a data is available from the EOL RELAMPAGO database (Arias & Chandrasekar, 2019). LMA and GLM data are available at the NASA Global Hydrometeorology Resource Center (Lang, 2020; Peterson, 2019a, 2019b). *GOES-16* Advanced Baseline Imager data is available on NCEI's Archive Information Request System (GOES-R Algorithm Working Group and GOES-R Series Program Office, 2018). ARM sounding data is available from ARM's Data Discovery (Keeler et al., 2022).

Acronyms and Abbreviations

AMF1	ARM mobile facility
ARM	Atmospheric Radiation Measurement
BSR	broad stratiform region

CACTI	Cloud, Aerosol, and Complex Terrain Interactions
CHIVO	CSU C-band radar
DCC	deep convective core
DWCC	deep and wide convective core
GLM	Geostationary Lightning Mapper
HID	hydrometeor identification
IOP	intensive observing period
IWP	ice water path
LCFA	Lightning Cluster and Filter Algorithm
LIS	Lightning Imager Sensor
LMA	Lightning Mapping Array
MCS	mesoscale convective system
MSL	mean sea level
NCAR	National Center for Atmospheric Research
OTD	Optical Transient Detector
PF	precipitation feature
PID	particle identification
PPI	plan position indicator
QC	quality-control
RELAMPAGO	Remote sensing of Electrification, Lightning, And Mesoscale/microscale Processes with Adaptive Ground Observations
RHI	range-height indicator
SDC	Sierras de Cordoba
SEC	sector
TRMM	Tropical Rainfall Measuring Mission
VHF	very high frequency
WCC	wide convective core

Acknowledgments

This research was supported by NSF grants AGS-1661657 and AGS-2146709, DOE grant DE-SC0022056, and a NASA FINESST Fellowship (NASA Grant 80NSSC21K1618). We thank Kyle Hilburn for his assistance with the parallax correction code, and Ivan Arias Hernandez, V. Chandrasekar, and Brenda Dolan for their assistance with processing the CHIVO dataset. We also thank Angela Rowe and Stacy Brodzik for their comments and discussions. Rachel Albrecht was supported by FAPESP (*Fundação de Amparo à Pesquisa do Estado de São Paulo*) Grant 2015/14497-0 and CNPq (*Conselho Nacional de Desenvolvimento Científico e Tecnológico*) grants 438638/2018-2 and 313355/2021-5.

References

Albrecht, R. I., Goodman, S. J., Buechler, D. E., Blakeslee, R. J., & Christian, H. J. (2016). Where are the lightning hotspots on Earth? *Bulletin of the American Meteorological Society*, *97*(11), 2051–2068. https://doi.org/10.1175/BAMS-D-14-00193.1

Arias, I., & Chandrasekar, V. (2019). *CSU C-Band Radar Data*. Version 1.0. UCAR/NCAR - Earth Observing Laboratory. https://doi.org/10.26023/DA1G-MCNC-YB0F

Arias, I., Chandrasekar, V., & Joshil, S. S. (2019). *Cross-validation of CSU-CHIVO radar and GPM during RELAMPAGO*. In *International Geoscience Remote Sensing Symposium* (pp. 7586–7589). IEEE. https://doi.org/10.1109/IGARSS.2019.8898835

Ávila, E. E., Bürgesser, R. E., Castellano, N. E., & Nicora, M. G. (2015). Diurnal patterns in lightning activity over South America. *Journal of Geophysical Research-Atmospheres*, *120*(8), 3103–3113. https://doi.org/10.1002/2014JD022965

Ávila, E. E., & Pereyra, R. G. (2000). Charge transfer during crystal-graupel collisions for two different cloud droplet size distributions. *Geophysical Research Letters*, *27*(23), 3837–3840. https://doi.org/10.1029/2000GL012302

Bell, M. M., Dixon, M., Lee, W.-C., Javornik, B., DeHart, J., Cha, T.-Y., & DesRosiers, A. (2022). nsf-lrose/lrose-topaz: lrose-topaz stable final release 20220222 (lrose-topaz-2022022). *Zenodo*. https://doi.org/10.5281/zenodo.6909479

Bruick, Z. S., Rasmussen, K. L., & Cecil, D. J. (2019). Subtropical South American hailstorm characteristics and environments. *Monthly Weather Review*, *147*(12), 4289–4304. https://doi.org/10.1175/MWRD-19-0011.1

Bruning, E. C., & MacGorman, D. R. (2013). Theory and observations of controls on lightning flash size spectra. *Journal of the Atmospheric Sciences*, *70*(12), 4012–4029. https://doi.org/10.1175/JAS-D-12-0289.1

Bruning, E. C., Rust, W. D., Schuur, T. J., MacGorman, D. R., Krehbiel, P. R., & Rison, W. (2007). Electrical and polarimetric radar observations of a multicell storm in TELEX. *Monthly Weather Review*, *135*(7), 2525–2544. https://doi.org/10.1175/MWR3421.1

Bruning, E. C., & Thomas, R. J. (2015). Lightning channel length and flash energy determined from moments of the flash area distribution. *Journal of Geophysical Research-Atmospheres*, *120*(17), 8925–8940. https://doi.org/10.1002/2015JD023766

Bruning, E. C., Tillier, C. E., Edgington, S. F., Rudlosky, S. D., Zajic, J., Gravelle, C., et al. (2019). Meteorological imagery for the geostationary lightning mapper. *Journal of Geophysical Research-Atmospheres*, *124*(24), 14285–14309. https://doi.org/10.1029/2019JD030874

Bruning, E. C., Weiss, S. A., & Calhoun, K. M. (2014). Continuous variability in thunderstorm primary electrification and an evaluation of inverted-polarity terminology. *Atmospheric Research*, *135*, 274–284. https://doi.org/10.1016/j.atmosres.2012.10.009

Cecil, D. J., & Blankenship, C. B. (2012). Toward a global climatology of severe hailstorms as estimated by satellite passive microwave imagers. *Journal of Climate*, *25*(2), 687–703. https://doi.org/10.1175/JCLI-D-11-00130.1

Christian, H. J., Blakeslee, R. J., Boccippio, D. J., Boeck, W. L., Buechler, D. E., Driscoll, K. T., et al. (2003). Global frequency and distribution of lightning as observed from space by the Optical Transient Detector. *Journal of Geophysical Research*, *108*(D1), 4005. https://doi.org/10.1029/2002JD002347

Deierling, W., Petersen, W. A., Latham, J., Ellis, S., & Christian, H. J. (2008). The relationship between lightning activity and ice fluxes in thunderstorms. *Journal of Geophysical Research*, *113*(D15), D15210. https://doi.org/10.1029/2007JD009700

Dolan, B., Rutledge, S. A., Lim, S., Chandrasekar, V., & Thurai, M. (2013). A robust C-band hydrometeor identification algorithm and application to a long-term polarimetric radar dataset. *Journal of Applied Meteorology and Climatology*, *52*(9), 2162–2186. https://doi.org/10.1175/JAMC-D-12-0275.1

Fuchs, B. R. (2017). *Microphysical, dynamical, and lightning processes associated with anomalous charge structures in isolated convection* (Ph. D. dissertation). Department of Atmospheric Science, Colorado State University.

Fuchs, B. R., Bruning, E. C., Rutledge, S. A., Carey, L. D., Krehbiel, P. R., & Rison, W. (2016). Climatological analyses of LMA data with an open-source lightning clustering algorithm. *Journal of Geophysical Research-Atmospheres*, *121*(14), 8625–8648. https://doi.org/10.1002/2015JD024663

GOES-R Algorithm Working Group and GOES-R Series Program Office. (2018). *NOAA GOES-R Series Advanced Baseline Imager (ABI) lLevel 2 Cloud Top Height (ACHA). [cloud top height]*. NOAA National Centers for Environmental Information. https://doi.org/10.7289/V5HX19ZQ

Goodman, S. J., Blakeslee, R. J., Koshak, W. J., Mach, D., Bailey, J., Buechler, D., et al. (2013). The GOES-R Geostationary Lightning Mapper (GLM). *Atmospheric Research*, *125–126*, 34–49. https://doi.org/10.1016/j.atmosres.2013.01.006

Heymsfield, A. J., & Miller, K. M. (1988). Water vapor and ice mass transported into the anvils of CCOPE thunderstorms: Comparison with storm influx and rainout. *Journal of the Atmospheric Sciences*, *45*(22), 3501–3514. https://doi.org/10.1175/1520-0469(1988)045<3501:WVAIMT>2.0.CO;2

Heymsfield, A. J., & Palmer, A. G. (1986). Relations for deriving thunderstorm anvil mass of CCOPE storm water budget estimates. *Journal of Climate and Applied Meteorology*, *25*(5), 691–702. https://doi.org/10.1175/1520-0450(1986)025<0691:RFDTAI>2.0.CO;2

Houze, R. A., Jr., Rasmussen, K. L., Zuluaga, M. D., & Brodzik, S. R. (2015). The variable nature of convection in the tropics and subtropics: A legacy of 16 years of the Tropical Rainfall Measuring Mission satellite. *Reviews of Geophysics*, *53*(3), 994–1021. https://doi.org/10.1002/2015RG000488

Houze, R. A., Jr., Wilton, D. C., & Smull, B. F. (2007). Monsoon convection in the Himalayan region as seen by the TRMM Precipitation Radar. *Quarterly Journal of the Royal Meteorological Society*, *133*(627), 1389–1411. https://doi.org/10.1002/qj.106

Keeler, E., Burk, K., & Kyrouac, J. (2022). Balloon-borne sounding system (BBSS), WNPN output data [Dataset]. Atmospheric Radiation Measurement (ARM) Archive, ARM Data Center, Oak Ridge National Laboratory (ORNL). https://doi.org/10.5439/1595321

Kummerow, C., Barnes, W., Kozu, T., Shiue, J., & Simpson, J. (1998). The Tropical Rainfall Measuring Mission (TRMM) sensor package. *Journal of Atmospheric and Oceanic Technology*, *15*(3), 809–817. https://doi.org/10.1175/1520-0426(1998)015,0809:TTRMMT.2.0.CO;2

Lang, T. J. (2020). Remote sensing of electrification, lightning, and mesoscale/microscale processes with adaptive ground observations (RELAMPAGO) lightning mapping array (LMA) [V1]. In *Dataset Available Online from the NASA Global Hydrometeorology Resource Center DAAC, Huntsville, Alabama, U.S.A*. https://doi.org/10.5067/RELAMPAGO/LMA/DATA101

Lang, T. J. (2023). Validation of the Geostationary Lightning Mapper with a lightning mapping array in Argentina: Implications for current and future spaceborne lightning observations. *Earth and Space Science*, *10*, e2023EA002998. https://doi.org/10.1029/2023EA002998

Lang, T. J., Ávila, E. E., Blakeslee, R. J., Burchfield, J., Wingo, M., Bitzer, P. M., et al. (2020). The RELAMPAGO lightning mapping array: Overview and initial comparison with the Geostationary Lightning Mapper. *Journal of Atmospheric and Oceanic Technology*, *37*(8), 1457–1475. https://doi.org/10.1175/JTECHD-20-0005.1

Liu, C., & Zipser, E. (2013). Regional variation of morphology of organized convection in the tropics and subtropics. *Journal of Geophysical Research-Atmospheres*, *118*(2), 453–466. https://doi.org/10.1029/2012JD018409

Liu, C., Zipser, E., Cecil, D. J., Nesbitt, S. W., & Sherwood, S. (2008). A cloud and precipitation feature database from nine years of TRMM observations. *Journal of Applied Meteorology and Climatology*, *47*(10), 2712–2728. https://doi.org/10.1175/2008JAMC1890.1

Mecikalski, R. M., Bain, A. L., & Carey, L. D. (2015). Radar and lightning observations of deep moist convection across Northern Alabama during DC3: 21 May 2012. *Monthly Weather Review*, *143*(7), 2774–2794. https://doi.org/10.1175/MWR-D-14-00250.1

Miller, L. J., & Fredrick, S. M. (1999). *SPRINT: Sorted Position Radar INTerpolation*. National Center for Atmospheric Research.

Nesbitt, S. W., Cifelli, R., & Rutledge, S. A. (2006). Storm morphology and rainfall characteristics of TRMM precipitation features. *Monthly Weather Review*, *134*(10), 2702–2721. https://doi.org/10.1175/MWR3200.1

Nesbitt, S. W., Salio, P. V., Ávila, E., Bitzer, P., Carey, L., Chandrasekar, V., et al. (2021). A storm safari in subtropical South America. *Bulletin of the American Meteorological Society*, *102*(8), 1621–1644. https://doi.org/10.1175/BAMS-D-20-0029.1

Nesbitt, S. W., Zipser, E. J., & Cecil, D. J. (2000). A census of precipitation features in the tropics using TRMM: Radar, ice scattering, and lightning observations. *Journal of Climate*, *13*(23), 4087–4106. https://doi.org/10.1175/1520-0442(2000)013,4087:ACOPFI.2.0.CO;2

Peterson, M. (2019a). Geostationary Lightning Mapper (GLM) Cluster Integrity, Exception Resolution and Reclustering Algorithm (CIERRA). In *Dataset Available Online from the NASA Global Hydrometeorology Resource Center DAAC, Huntsville, Alabama, U.S.A*. https://doi.org/10.5067/GLM/CIERRA/DATA101

Peterson, M. (2019b). Research applications for the Geostationary Lightning Mapper operational lightning flash data product. *Journal of Geophysical Research-Atmospheres*, *124*(17–18), 10205–10231. https://doi.org/10.1029/2019JD031054

Peterson, M. (2021a). Holes in optical lightning flashes: Identifying poorly transmissive clouds in lightning imager data. *Earth and Space Science*, *8*(2), e2020EA001294. https://doi.org/10.1029/2020EA001294

Peterson, M. (2021b). Where are the most extraordinary lightning megaflashes in the Americas? *Bulletin of the American Meteorological Society*, *102*(3), E660–E671. https://doi.org/10.1175/BAMS-D-20-0178.1

Peterson, M., Mach, D., & Buechler, D. (2021). A global LIS/OTD climatology of lightning Flash Extent Density. *Journal of Geophysical Research-Atmospheres*, *126*(8), e2020JD033885. https://doi.org/10.1029/2020JD033885

Peterson, M. J., Lang, T. J., Bruning, E. C., Albrecht, R., Blakeslee, R. J., Lyons, W. A., et al. (2020). New World Meteorological Organization certified megaflash lightning extremes for flash distance (709 km) and duration (16.73 s) recorded from space. *Geophysical Research Letters*, *47*(16), e2020GL088888. https://doi.org/10.1029/2020GL088888

Proctor, D. E. (1971). A hyperbolic system for obtaining VHF radio pictures of lightning. *Journal of Geophysical Research*, *76*(6), 1478–1489. https://doi.org/10.1029/JC076i006p01478

Rasmussen, K. L., Chaplin, M. M., Zuluaga, M. D., & Houze, R. A., Jr. (2016). Contribution of extreme convective storms to rainfall in South America. *Journal of Hydrometeorology*, *17*(1), 353–367. https://doi.org/10.1175/JHM-D-15-0067.1

Rasmussen, K. L., & Houze, R. A., Jr. (2011). Orogenic convection in subtropical SouthSouth America as seen by the TRMM satellite. *Monthly Weather Review*, *139*(8), 2399–2420. https://doi.org/10.1175/MWR-D-10-05006.1

Rasmussen, K. L., & Houze, R. A., Jr. (2016). Convective initiation near the Andes in subtropical South America. *Monthly Weather Review*, *144*(6), 2351–2374. https://doi.org/10.1175/MWR-D-15-0058.1

Rasmussen, K. L., Zuluaga, M. D., & Houze, R. A., Jr. (2014). Severe convection and lightning in subtropical South America. *Geophysical Research Letters*, *41*(20), 7359–7366. https://doi.org/10.1002/2014GL061767

Reynolds, S. E., Brook, M., & Gourley, M. F. (1957). Thunderstorm charge separation. *Journal of the Atmospheric Sciences*, *14*(5), 426–436. https://doi.org/10.1175/1520-0469(1957)014<0426:TCS>2.0.CO;2

Rison, W., Thomas, R., Krehbiel, P., Hamlin, T., & Harlin, J. (1999). A GPS-based three-dimensional lightning mapping system: Initial observations in central New Mexico. *Geophysical Research Letters*, *26*(23), 3573–3576. https://doi.org/10.1029/1999GL010856

Rocque, M. N. (2023). *Influence of terrain on the characteristics and life cycle of convection observed in subtropical South America*. (Ph.D. dissertation). Department of Atmospheric Science, Colorado State University. Retrieved from https://hdl.handle.net/10217/236992

Rocque, M. N., & Rasmussen, K. L. (2022). The impact of topography on the environment and lifecycle of weakly- and strongly-forced MCSs during RELAMPAGO. *Monthly Weather Review*, *150*(9), 2317–2338. https://doi.org/10.1175/MWR-D-22-0049.1

Romatschke, U., & Houze, R. A., Jr. (2010). Extreme summer convection in South America. *Journal of Climate*, *23*(14), 3761–3791. https://doi.org/10.1175/2010JCLI3465.1

Rudlosky, S. D., Goodman, S. J., Virts, K. S., & Bruning, E. C. (2019). Initial Geostationary Lightning Mapper observations. *Geophysical Research Letters*, *46*(2), 1097–1104. https://doi.org/10.1029/2018GL081052

Rutledge, S. A., Hilburn, K. A., Clayton, A., Fuchs, B., & Miller, S. D. (2020). Evaluating Geostationary Lightning Mapper flash rates within intense convective storms. *Journal of Geophysical Research-Atmospheres*, *125*(14), e2020JD032827. https://doi.org/10.1029/2020JD032827

Saunders, C. P. R., & Peck, S. L. (1998). Laboratory studies of the influence of the rime accretion rate on charge transfer during graupel/crystal collisions. *Journal of Geophysical Research*, *103*(D12), 13949–13956. https://doi.org/10.1029/97JD02644

Schmidt, T. J., Griffith, P., Gunshor, M. W., Daniels, J. M., Goodman, S. J., & Lebair, W. J. (2017). A closer look at the ABI on the GOES-R series. *Bulletin of the American Meteorological Society*, *98*(4), 681–698. https://doi.org/10.1175/BAMS-D-15-00230.1

Steiner, M., Houze, R. A., Jr., & Yuter, S. E. (1995). Climatological characterization of three-dimensional storm structure from operational radar and rain gauge data. *Journal of Applied Meteorology*, *34*(9), 1978–2007. https://doi.org/10.1175/1520-0450(1995)034,1978:CCOTDS.2.0.CO;2

Stolzenburg, M., Marshall, T. C., Rust, W. D., & Smull, B. F. (1994). Horizontal distribution of electrical and meteorological conditions across the stratiform region of a mesoscale convective system. *Monthly Weather Review*, *122*(8), 1777–1797. https://doi.org/10.1175/1520-0493(1994)122<1777:HDOEAM>2.0.CO;2

Stolzenburg, M., Rust, W. D., Smull, B. F., & Marshall, T. C. (1998). Electrical structure in thunderstorm convective regions. 1. Mesoscale convective systems. *Journal of Geophysical Research-Atmospheres*, *103*(D12), 14059–14078. https://doi.org/10.1029/97JD03546

Takahashi, T. (1978). Riming electrification as a charge generation mechanism in thunderstorms. *Journal of the Atmospheric Sciences*, *35*(8), 1536–1548. https://doi.org/10.1175/1520-0469(1978)035<1536:REAACG>2.0.CO;2

Thomas, R. J., Krehbiel, P. R., Rison, W., Hunyady, S. J., Winn, W. P., Hamlin, T., & Harlin, J. (2004). Accuracy of the lightning mapping array. *Journal of Geophysical Research*, *109*(D14), D14207. https://doi.org/10.1029/2004JD004549

Varble, A. C., Nesbitt, S. W., Salio, P., Hardin, J. C., Bharadwaj, N., Borque, P., et al. (2021). Utilizing a storm-generating hotspot to study convective cloud transitions. *Bulletin of the American Meteorological Society*, *102*(8), E1597–E1620. https://doi.org/10.1175/BAMS-D-20-0030.1

Vera, C., Baez, J., Douglas, M., Emmanuel, C. B., Marengo, J., Meitin, J., et al. (2006). The South American low-level jet experiment. *Bulletin of the American Meteorological Society*, *87*(1), 63–77. https://doi.org/10.1175/BAMS-87-1-63

Vicente, G. A., Davenport, J. C., & Scofield, R. A. (2002). The role of orographic and parallax corrections on real time high resolution satellite rainfall rate distribution. *International Journal of Remote Sensing*, *23*(2), 221–230. https://doi.org/10.1080/01431160010006935

Vivekanandan, J., Zrnic, D. S., Ellis, S. M., Oye, R., Ryzhkov, A. V., & Straka, J. (1999). Cloud microphysics retrieval using S-band dual-polarization radar measurements. *Bulletin of the American Meteorological Society*, *80*(3), 381–388. https://doi.org/10.1175/1520-0477(1999)080<0381:CMRUSB>2.0.CO;2

Williams, E. R., Rutledge, S. A., Geotis, S. G., Renno, N., Rasmussen, E., & Rickenbach, T. (1992). A radar and electrical study of tropical "Hot Towers". *Journal of the Atmospheric Sciences*, *49*(15), 1386–1395. https://doi.org/10.1175/1520-0469(1992)049<1386:ARAESO>2.0.CO;2

Zipser, E. J., Cecil, D. J., Liu, C., Nesbitt, S. W., & Yorty, D. P. (2006). Where are the most intense thunderstorms on Earth? *Bulletin of the American Meteorological Society*, *87*(8), 1057–1071. https://doi.org/10.1175/BAMS-87-8-1057

Zipser, E. J., & Lutz, K. R. (1994). The vertical profile of radar reflectivity of convective cells: A strong indicator of storm intensity and lightning probability? *Monthly Weather Review*, *122*(8), 1751–1759. https://doi.org/10.1175/1520-0493(1994)122<1751:TVPORR>2.0.CO;2

Zuluaga, M. D., & Houze, R. A., Jr. (2013). Evolution of the population of precipitating convective systems over the equatorial Indian Ocean in active phases of the Madden–Julian oscillation. *Journal of the Atmospheric Sciences*, *70*(9), 2713–2725. https://doi.org/10.1175/JAS-D-12-0311.1